Published in final edited form as:

Structure. 2016 September 06; 24(9): 1488–1498. doi:10.1016/j.str.2016.06.017.

Structural Basis for Receptor Recognition by the Human CD59-Responsive Cholesterol-Dependent Cytolysins

Sara L. Lawrence[1], **Michael A. Gorman**[1], **Susanne C. Feil**[1], **Terrence D. Mulhern**[2], **Michael J. Kuiper**[3], **Adam J. Ratner**[4], **Rodney K. Tweten**[5], **Craig J. Morton**[1,6], and **Michael W. Parker**[1,2,6,*]

[1]ACRF Rational Drug Discovery Centre, St. Vincent's Institute of Medical Research, Fitzroy, VIC 3065, Australia

[2]Department of Biochemistry and Molecular Biology, Bio21 Molecular Science and Biotechnology Institute, The University of Melbourne, Parkville, VIC 3010, Australia

[3]Victorian Life Sciences Computation Initiative, The University of Melbourne, Parkville, VIC 3010, Australia

[4]Departments of Pediatrics and Microbiology, New York University School of Medicine, New York, NY 10016, USA

[5]Department of Microbiology and Immunology, University of Oklahoma, Health Sciences Center, Oklahoma City, OK 73104, USA

SUMMARY

Cholesterol-dependent cytolysins (CDCs) are a family of pore-forming toxins that punch holes in the outer membrane of eukaryotic cells. Cholesterol serves as the receptor, but a subclass of CDCs first binds to human CD59. Here we describe the crystal structures of vaginolysin and intermedilysin complexed to CD59. These studies, together with small-angle X-ray scattering, reveal that CD59 binds to each at different, though overlapping, sites, consistent with molecular dynamics simulations and binding studies. The CDC consensus undecapeptide motif, which for the CD59-responsive CDCs has a proline instead of a tryptophan in the motif, adopts a strikingly different conformation between the structures; our data suggest that the proline acts as a selectivity switch to ensure CD59-dependent CDCs bind their protein receptor first in preference to

*Correspondence: mparker@svi.edu.au.
[6]Co-senior author

ACCESSION NUMBERS

The structures have been deposited in the PDB (http://www.rcsb.org/pdb/) under the accession numbers PDB: 5IMW, 5IMT, and 5IMY for ILY^{ml}, ILY^{ml}-$CD59^{D22A}$, and VLY^{ml}-$CD59^{D22A}$, respectively.

SUPPLEMENTAL INFORMATION

Supplemental Information includes Supplemental Experimental Procedures, six figures, and one table and can be found with this article online at http://dx.doi.org/10.1016/j.str.2016.06.017.

AUTHOR CONTRIBUTIONS

M.W.P., A.J.R., and R.K.T. conceived the project. S.L.L. expressed, purified and, with S.C.F., crystallized proteins. S.L.L., S.C.F., C.J.M., and M.A.G. collected and processed X-ray diffraction data. C.J.M. and S.C.F. determined and refined crystal structures. S.L.L. prepared samples for SAXS analysis and, with T.D.M., collected SAXS data and analyzed it. S.L.L. performed the binding studies. M.J.K. performed MD simulations and, with C.J.M., analyzed the data. C.J.M. and M.W.P. wrote the manuscript, and all authors contributed to revisions.

cholesterol. The structural data suggest a detailed model of how these water-soluble toxins assemble as prepores on the cell surface.

Graphical Abstract

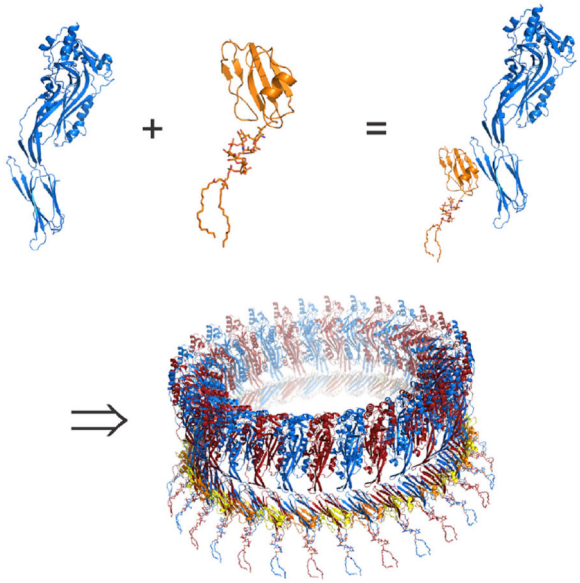

INTRODUCTION

Cholesterol-dependent cytolysins (CDCs) are a family of poreforming toxins, consisting of more than 40 known members, which contribute to the pathogenesis of a wide variety of disease-causing bacteria (Tweten, 2005). CDCs are secreted as water-soluble monomers that recognize and bind mammalian cells before assembling into prepores of >30 monomers on the surface of cholesterol-rich membranes. Upon completion of the prepore the monomers collectively undergo a structural transition that facilitates a 40-Å vertical collapse toward the membrane surface, whereupon two α-helical segments from each monomer unfurl and insert into the membrane as β hairpins (Shatursky et al., 1999; Shepard et al., 1998). The resultant β-barrel pore has a diameter of ~300 Å, causing lysis of the target cell (Tilley et al., 2005).

Domain 4 (D4) is the membrane-sensing domain of CDCs (Figure 1) with cholesterol thought to be the receptor for many (Giddings et al., 2003). The L1 loop at the tip of D4 has been identified as a recognition site for cholesterol (Farrand et al., 2010). CDCs also contain a highly conserved undecapeptide (UDP) sequence in another loop at the tip of D4, and this region forms an interaction site with membranes (Ramachandran et al., 2002). The UDP is a key element in the allosteric pathway that couples membrane binding in D4 to the conformational changes that have to occur in D3 for the conversion of the prepore to pore (Dowd et al., 2012). Another loop at the tip of D4, the L3 loop, acts as a lipid sensor (Farrand et al., 2015). More recently, it has been reported that at least two CDCs bind certain glycans (Shewell et al., 2014). The putative binding site was suggested to be around the UDP loop based on mutagenesis studies. A subset of CDCs have been shown to use human

CD59, a glycosyl phosphatidylinositol anchored protein, as their receptor (Giddings et al., 2004).

The known CD59-responsive CDCs are intermedilysin (ILY) from *Streptococcus intermedius*, vaginolysin (VLY) from *Gardnerella vaginalis*, and lectinolysin (LLY) from *Streptococcus mitis*, with CDCs from *Streptococcus tigurinus* and *Streptococcus pseudopneumoniae* predicted to be CD59 responsive due to the presence of a conserved D4 motif only present in CD59-binding CDCs (Wade et al., 2015). These CDCs have been considered atypical because of their preference for human cells (Gelber et al., 2008; Nagamune et al., 1996; Tabata et al., 2014; Zvirbliene et al., 2010), in contrast to the majority of CDCs that can lyse most eukaryotic cells. ILY is strictly specific for human cells (Nagamune et al., 1996), whereas VLY can bind to non-human cells providing they are cholesterol rich (Zilnyte et al., 2015), and LLY may behave similarly (Tabata et al., 2014). However, VLY is ~100-fold less efficient in lysing non-human cells compared with human cells (Zilnyte et al., 2015). Although ILY does not bind to cholesterol-rich cell membranes in the absence of CD59, it does bind well to cholesterol-rich liposomes via loop L1 (Dowd et al., 2012). CDC binding to CD59 initiates a series of conformational changes leading to oligomerization (LaChapelle et al., 2009; Soltani et al., 2007). During the assembly of the prepore complex CD59 remains bound but dissociates when the prepore is converted to a pore (LaChapelle et al., 2009). The CD59-responsive CDCs still require cholesterol for membrane insertion of the prepore complex, and the primary structure of the UDP loop is critical for prepore-to-pore conversion (Giddings et al., 2003; Polekhina et al., 2005). The CD59-dependent CDCs also exhibit atypical UDP-loop sequences: in VLY and LLY the consensus motif, ECTGLAWEWWR, becomes EKTGLVWEPWR, whereas in ILY there are alternative changes to GATGLAWEPWR. Mutation of the proline residue in VLY to the consensus tryptophan residue results in a toxin that can no longer form pores (Gelber et al., 2008) whereas the reverse mutation, Trp to Pro, in the typical CDC pneumolysin (PLY), causes a significant drop in activity (Gelber et al., 2008).

Wickham et al. (2011) proposed a CD59 recognition motif (Y-X-Y-X_{14}-R-S) in D4 of the CD59-responsive CDCs. A recent low-resolution (3.5 Å) partially refined structure of the ILY-CD59 complex supports elements of this binding site but does not fully explain the mutagenesis results and suggested a secondary CD59 binding site (Johnson et al., 2013). Here we report the crystal structures of a monomer-locked VLY mutant (VLY^{ml}) bound to CD59 mutant D22A ($CD59^{D22A}$) as well as well-refined structures of a monomer-locked mutant of ILY, alone and in complex with $CD59^{D22A}$. Our structures, supported by small-angle X-ray scattering studies, reveal a single binding site for CD59 on each CDC monomer, although the detailed interactions show some variation. A comparative study of all available CDC crystal structures, together with published biochemical data, suggests a role for the CD59-specific proline in the UDP loop and multiple roles that the UDP loop plays in the different stages of conversion from water-soluble toxin to membrane pore.

RESULTS

VLY^{ml} Recognizes CD59^{D22A} via the β Tongue of D4

Despite extensive efforts, we could not generate a stable complex with wild-type VLY suitable for structural studies. It is possible that receptor engagement may have induced conformational changes associated with the formation of membrane-bound oligomers. However, a "monomer-locked" version of VLY, with an engineered disulfide that minimizes monomer-monomer interactions in the soluble form, did give a stable complex with CD59. The mutant design was based on a similar ILY mutant (LaChapelle et al., 2009), which prevents the disengagement of strand b5 from b4 in D3, a key step associated with the formation of membrane-bound oligomers. VLY^{wt} residues Thr333 and Ile348 were mutated to cysteines to generate the disulfide bridge between β strands 4 and 5 in D3. For the structural studies we used a modified CD59 (D22A), as this protein has been shown previously to bind with higher affinity to ILY (Wickham et al., 2011).

The VLY^{ml}-CD59^{D22A} complex was crystallized and its structure determined by molecular replacement to a resolution of 2.4 A (Table 1). VLY^{ml} adopts the canonical CDC fold (Rossjohn et al., 1997) with maximal dimensions of 120 × 52 × 30 Å (Figure 1A). It is composed of four domains: D1 (residues 47–66, 103–192, 243–288, and 364–387) consists of three α helices and one β sheet, D2 (residues 67–102 and 388–405) contains one β sheet, D3 (residues 193–242 and 289–363) is composed of a five-stranded anti-parallel β sheet that is surrounded by the two α-helical bundles that become transmembrane hairpins TMH1 (residues 204–231) and TMH2 (residues 302–325), and D4 (residues 406–510) is folded into a compact β sandwich. D2 is connected to D4 by a single glycine linker. An electrostatic calculation shows that one face of the molecule is very electropositive whereas the opposing face is exceptionally electronegative; this is unusual for CDCs but would presumably help guide the assembly of the VLY^{ml} oligomer (Figure S1B).

CD59^{D22A} binds to D4 of VLY^{ml} in a manner analogous to the published "primary" interaction with ILY^{EPP} (identical to the monomer-locked ILY [ILY^{ml}] described here) (Figures 1A, 2A, 2C, andS2) (Johnson et al., 2013). The interaction with VLY^{ml} occurs primarily through the β tongue of D4, and is stabilized by backbone hydrogen bonds (two between V437 and C63, one between S439 and Y61) between the second strand of the β tongue and the last strand in CD59^{D22A}, forming an extended β sheet between the two proteins. Further hydrogen bonds occur between side chains including D425 to Y61, R438 to Q74, and R440 to E76. Water-mediated hydrogen bonds are present between Y423 and D57 (CD59^{D22A}), D425 and N46 and F47 (CD59^{D22A}), and E430 and Y62 (CD59^{D22A}). In total, ten residues from VLY^{ml} make direct contact with 14 different CD59^{D22A} residues (Figure 2A). Noteworthy van der Waals (vdW) contacts are a ring stack between Y423 and F47 (CD59^{D22A}) and the insertion of V437 into a hydrophobic pocket of CD59^{D22A} formed by F42, Y62, and the C45-C63 disulfide. The buried surface area in the interface is relatively small (~680 Å^2, being 329 Å^2 from VLY^{ml} and 353 Å^2 from CD59^{D22A}) but shows high surface complementarity, with an Sc value of 0.73 (Lawrence and Colman, 1993).

Monomer-Locked Structure of ILY Resembles Closely the Wild-Type Structure

Although the crystal structure of wild-type ILY (ILY^{wt}) was published by us some years ago (Polekhina et al., 2005), we wanted to determine the structure of the monomer-locked form (LaChapelle et al., 2009) required to form a stable CD59 complex (see Supplemental Information), so as to directly compare the toxin's structure in the absence or presence of CD59. The mutant ILY^{ml} crystallized under wild-type conditions and the structure was determined by molecular replacement (Supplemental Experimental Procedures, Figure S3B, and Table 1). Two molecules were located in the asymmetric unit and superimposed closely with a root-mean-square deviation (rmsd) of 0.5 Å on α carbon atoms. The structures of both monomers in the mutant are closer to the structure of chain A in the wild-type structure (0.8 Å and 0.9 Å rmsd) than to chain B (1.2 Å and 1.4 Å) due to a rotation of D4 in chain B of the wild-type structure.

ILY^{ml} Does Not Undergo Any Significant Conformational Changes on Binding $CD59^{D22A}$

The crystal structure of the complex of ILY^{ml} and $CD59^{D22A}$ was determined by molecular replacement to 2.7-Å resolution (Supplemental Experimental Procedures, Figure S3A, and Table 1). One molecule of a 1:1 complex was located in the asymmetric unit with the $CD59^{D22A}$ molecule binding to ILY^{ml} in the same location as previously described (Figures 1B and 1D) (Johnson et al., 2013). The structure of ILY^{ml} in the complex is very similar to uncomplexed ILY seen for both ILY^{wt} and the monomer-locked mutant. Superposition of domains 1–3 of the uncomplexed ILY^{ml} monomers onto the complexed structure results in a rmsd on the α carbons of 1.0 Å, with each separate domain superimposing individually with similar rmsd. However, complexed ILY^{ml} is more elongated than free ILY^{ml} due to a rotation of D4 by ~13° with respect to D1 to D3 in the former. Whether this D4 shift is due to $CD59^{D22A}$ binding is difficult to determine, as there is a significant alteration in the overall orientation of proteins within the crystal lattice going from the free ILY^{ml} structures to the ILY^{ml}-$CD59^{D22A}$ complex. With regard to localized changes, very few were noted that could not be ascribed to crystal lattice effects.

The crystals of the ILY^{ml}-$CD59^{D22A}$ complex reported here diffract to significantly higher resolution (2.7 Å) than the published structure (PDB: 4BIK, 3.5 Å resolution) and belong to a different space group. Nevertheless, comparison of the two structures shows that the ILY^{ml} domains superimpose closely (a carbon rmsd for D1 to D4 being 0.8 Å, 1.2 Å, 0.9 Å, and 0.6 Å, respectively) as does $CD59^{D22A}$ (rmsd of 0.6 Å). Rotations of D4, likely due to crystal packing effects, are seen between the two structures, so that overall rsmd are significantly larger. Although there are some differences in residue interactions between the structures, these can all be explained by crystal lattice effects. The packing between adjacent proteins in the published structure (PDB: 4BIK) gives rise to linear oligomers of the ILY^{ml}-$CD59^{D22A}$ complex, which bring adjacent $CD59^{D22A}$ molecules into contact with the β tongue in D4 of ILY^{ml}, creating a secondary binding site. The most significant impact of this packing arrangement is the positioning of the R451 and R453 side chains, which form interactions with R55 and E57 of the adjacent $CD59^{D22A}$ in the published structure, while in our structure R453 does not interact with $CD59^{D22A}$ at all and R451 is involved in a network of hydrogen bonds and vdW contacts with Q74, Y61, and Y62.

Solution Structure of ILY^{ml}-CD59^{D22A} Confirms a 1:1 Complex

Our structure of the ILY^{ml}-CD59^{D22A} complex showed only one CD59^{D22A} molecule bound to ILY^{ml}, in contrast to the findings of Johnson et al. (2013), who reported interactions between adjacent proteins in the crystal giving rise to a secondary CD59 interaction. We therefore carried out small-angle X-ray scattering (SAXS) measurements of the complex to confirm the stoichiometry of the complex in solution (Supplemental Experimental Procedures, Table S1, and Figure S4). Ab initio shape envelope reconstructions yielded an average, filtered shape envelope that overlays well with our crystallographic model of the ILY^{ml}-CD59^{D22A} complex (Figure 3). The theoretical scattering profile generated from the coordinates of the ILY^{ml}-CD59^{D22A} crystallographic model was fitted to the static SAXS (Figure S4A). The fit was very good ($\chi_{CRTSOL} = 0.845$; $P_{\chi}(\chi^2; \nu) > 0.999$). The fit of all alternative crystallographic 1:1 and 1:2 ILY^{ml}-CD59 models, from the previously published ILY^{ml}-CD59 structure (PDB: 4BIK) (Johnson et al., 2013), were significantly worse (in all cases $\chi_{CRYSOL} > 1.182$; $P_F(F; \nu_1, \nu_2) < 1.2 \times 10^{-9}$). These analyses indicate that the crystallographic model determined here is an excellent representation of the solution structure of the ILY^{ml}-CD59^{D22A} complex.

VLY and ILY Bind CD59^{D22A} with Different Affinities

Microscale thermophoresis was used to measure the affinity of CD59^{D22A} for ILY^{wt} and VLY^{wt} in solution under identical experimental conditions. CD59^{D22A} bound ILY^{wt} with a K_D of 367 ± 46 nM, its affinity for VLY^{wt} was found to be approximately 2-fold lower with a K_D of 779 ± 30 nM ($p < 0.0001$) (Figure S5).

VLY^{ml} and ILY^{ml} Do Not Recognize CD59^{D22A} in Identical Fashion

As with the VLY^{ml}-CD59^{D22A} complex, the interaction between ILY^{ml} and CD59^{D22A} is stabilized by main-chain hydrogen bonds between β strand 2 of the β hairpin in D4 of ILY^{ml} and the last strand of the β sheet in CD59^{D22A} (E448 to K65, I450 to C63, S452 to Y61) resulting in an extended β sheet between the two molecules (Figures 2D and S2). Additional hydrogen bonds include R477 and C45, E438 and F47, S452 and Y61 and Y62, E445 and K66, and R451 and Q74. There are numerous water-mediated hydrogen bonds between the two proteins, more than seen for the VLY^{ml}-CD59^{D22A} complex, including from ILY^{ml} residues D502 and E438 to CD59^{D22A} residue N48 and a network involving L59 of CD59^{D22A} with S452, R430, and S454 of ILY^{ml}. In total, ten ILY^{ml} residues make contact with 13 residues in CD59^{D22A} (Figure 2D), including the packing of the I450 side chain into a CD59^{D22A} pocket formed by F42, Y62, and the C45-C63 disulfide as seen for V437 in VLY^{ml}. A similar amount of protein surface is buried in the ILY^{ml}-CD59^{D22A} interface to that in the VLY^{ml} complex, ~680 Å^2 with a surface complementarity of 0.70 (Lawrence and Colman, 1993).

Detailed comparison of the VLY^{ml} and ILY^{ml} interactions with CD59^{D22A} highlights differences in CD59 binding by these two CDCs. As noted above, in both cases the interaction between the CDC and CD59 occurs through the β tongue of D4 and buries a similar amount of protein surface. However, CD59^{D22A} binds lower down on the β tongue of VLY^{ml} and, hence, the finer details of the interaction are different between the two CDCs (Figure 2). In the VLY^{ml} complex the tip of the hairpin tilts away from CD59^{D22A} so that

there are no contacts from residues in the loop between the two strands. In ILY^{ml} a salt bridge is present between E445 in the hairpin loop and R66 in $CD59^{D22A}$. The start of the β tongue is packed more closely to $CD59^{D22A}$ in the VLY^{ml} complex than in the ILY^{ml}, with $CD59^{D22A}$ shifted toward the top of the hairpin on ILY^{ml} such that the first tyrosine in the putative CD59 recognition motif Y-X-Y-X14-R-S (Wickham et al., 2011) is 5.5 Å further away from $CD59^{D22A}$ in ILY^{ml} (Y434) than in VLY^{ml} (Y421). This shift means that a ring stack in the VLY^{ml} complex between Y421 and F47 in $CD59^{D22A}$ is replaced by a cation-π interaction with the guanidinium group of R480 in ILY^{ml}. The R480 side chain folds into the space between the shifted hairpin strand and $CD59^{D22A}$, to be sandwiched between F47 and the second tyrosine of the Y-X-Y sequence, Y436. The equivalent residue in VLY^{ml}, R467, is turned out toward solvent, away from the aromatic interaction, though packing partially against the stacked rings. In effect, the bend of the D4 β hairpin away from $CD59^{D22A}$ in the ILY^{ml} complex results in a more compact central contact surface, with the VLY^{ml} complex containing more interactions through the hairpin (Figure 2). This observation is not in disagreement with the very similar buried surface areas discussed previously, as ILY^{ml} makes additional peripheral contacts from the edge of other loops in D4 (e.g., R477, N501, D502) that are not present in the VLY^{ml} complex.

Interactions with the other residues in the CD59 recognition motif are conserved between the VLY^{ml} and ILY^{ml} complexes (Wickham et al., 2011). The RS pair (residues R438 and S439 in VLY^{ml} and R451 and S452 in ILY^{ml}) is on the β hairpin, with the serine forming both backbone and side-chain hydrogen bonds to the backbone of Y61 in $CD59^{D22A}$ (Figures 2C and 2F). Conservation of the serine is necessitated by the need to form side-chain interactions while remaining packed between each CDC and its bound $CD59^{D22A}$. The arginine side chain forms hydrogen bonds with the backbone carbonyl oxygen of Q74 toward the end of $CD59^{D22A}$, stabilizing the position of the $CD59^{D22A}$ C terminus with respect to the CDC (Figures 2C and 2F). Again, conservation of the arginine is implicit in this interaction, as no other amino acid would be able to reach across to form this stabilizing hydrogen-bonding arrangement. A comparison of the free and complexed ILY^{ml} structures reveals no significant rearrangements of the aforementioned side chains.

The mutagenesis studies also revealed that aromatic residues in $CD59^{D22A}$ (F42, F47, and Y62) play a key role in binding to ILY (Wickham et al., 2011) with double alanine mutations of F42, F47 or F42, and Y62 completely eliminating binding. Our crystal structures show that all these residues are involved in vdW contacts at the interface between the CDC and CD59 (Figure 2 and see above).

Molecular Dynamics Simulations Reveal Additional Interactions between CDC and CD59

Molecular dynamics (MD) simulations of both CDC-CD59 complexes indicate that the two different CD59-toxin interfaces are dynamically stable. In VLY^{ml}, the aromatic stack formed by F47 of $CD59^{D22A}$ with Y423 of VLY^{ml} (Figure 2B) is further stabilized during the simulation by rearrangement of VLY^{ml} residues Y421 and W481, such that Y421 forms an end-on ring interaction with F47 and W481 closes the aromatic box thus formed through another edge-face interaction with Y421 (Figure S6A). For ILY^{ml}, the cation-π stacking of the guanidinium group of R480 between F47 and Y436 (Figure 2E) is dynamic, with the

R480 side chain occasionally rearranging to salt bridge with nearby negatively charged residues, usually E438. The most stable arrangement of the ILY^{ml}-$CD59^{D22A}$ interface, Y436, orients such that a salt bridge is formed with E58 from $CD59^{D22A}$ (which points away from R480 in the crystal structure). At no point during the simulations has CDC dissociated from $CD59^{D22A}$, nor has the $CD59^{D22A}$ moved between the two binding positions to create a VLY^{ml}-like interface on ILY^{ml} or vice versa.

Movements of the CDC D4-D2 Interface in VLY^{ml}

Comparison of the VLY^{ml}-$CD59^{D22A}$ and ILY^{ml}-$CD59^{D22A}$ complex structures shows a clear difference between the arrangements of the domains in the two CDCs (Figure 1). When the proteins are superimposed over D1 to D3, D4 has undergone a substantial twist in VLY^{ml} when compared with ILY^{ml}. The movement is sufficient to bring the β tongue of D4 from one side of D2 in ILY^{ml} across to the other side of D2 in VLY^{ml} (cf. Figures 1C and 1D, a distance of more than 20 Å. The twist is stabilized in the VLY^{ml}-$CD59^{D22A}$ crystal by the packing between the two VLY^{ml} chains in the asymmetric unit (Figure S1). Although we cannot rule out crystal lattice forces as the origin of the marked twist, the structural rearrangement, if real, has implications for the formation of oligomeric CDC complexes and progression to the prepore state (see below). MD simulations of the VLY^{ml}-$CD59^{D22A}$ complex show that VLY^{ml} reverts to an ILY^{ml}-like conformation in which there is no twist apparent, suggesting that the dimer seen in the crystal is stabilizing a high-energy state.

The Conformation of the UDP Loop in CD59-Dependent CDCs Is Not Conserved

A key functional element of the CDCs is the UDP loop in D4 (Figures 1 and 2). The conformation of this loop is variable in the CDCs for which structures have been determined, being packed tightly against the rest of the domain in perfringolysin O (PFO) but occupying a range of more extended conformations in other CDCs (Figure 4). This conformational flexibility may play a role in the transmission of signals from D4 to the rest of the protein that indicate binding to a target membrane has occurred.

In the CD59-dependent CDCs there is a strictly conserved proline in the UDP loop instead of the tryptophan found in other CDCs. In the ILY^{ml} structure the presence of the proline promotes the neighboring arginine and glutamic acid residues to point out into solution, whereas in typical CDCs such as PFO the arginine hydrogen bonds to the backbone of the cholesterol-binding L1 loop. In the free ILY^{ml} structure the conformation of the UDP is only visible in one monomer in the asymmetric unit. The UDP structure for ILY^{ml} closely matches that of the wild-type ILY^{wt} B chain, which itself shows minimal difference to the ILY^{ml} free A chain (Figure 4A). In the ILY^{ml}-$CD59^{D22A}$ complex the UDP conformation is identical to the free ILY^{ml} A chain (Figure 4A). This consistency of UDP conformation suggests that there is a preferred orientation for the UDP loop in ILY^{ml} that is more extended than is seen for PFO.

In VLY^{ml}, however, the UDP varies significantly between the two monomers in the asymmetric unit (Figures 4B and 4C). Chain B of the VLY^{ml}-$CD59^{D22A}$ complex has a UDP-loop structure that is very similar to the ILY^{ml}-$CD59^{D22A}$ complex and free ILY^{ml} A chain (Figure 4C). In chain A of the VLY^{ml} complex, the loop curls up more closely toward

the rest of D4, with a maximum displacement relative to chain B of 9.4 Å at V477 (Figure 4B). This movement brings V477 closer to the body of D4, with the V477 to W481 distance reducing from 12.3 Å to 4.6 Å. A key difference between the two loop conformations is the presence, in the extended chain B conformation, of a stabilizing salt bridge between E479 and R482 at the C-terminal end of the UDP (Figure 4C). In chain A the E479 side-chain has swung down away from R482, moving 9 Å and freeing the R482 side chain to reorient toward the L1 loop, where it forms a hydrogen bond with the backbone carbonyl oxygen of L505 from the cholesterol-recognition motif.

In summary, superimposing D4 of the large number of non-CD59 dependent CDCs now available reveals that, with the exception of PFO, the UDP motif adopts a similar extended conformation with the key arginine residue of the motif pointing toward the backbone of the L1 cholesterol-sensing loop. In contrast, the key arginine residue in ILY points out to solution (in all seven available structures) even though the UDP adopts a conformation similar to that of all CDCs except PFO. Since the only sequence difference close by is the proline residue in ILY that replaces the tryptophan in the other CDCs, it follows that the role of the proline is to favor the breakage of the interaction between the UDP and L1 loops. Surprisingly, the two structures of VLY^{ml} show that it can adopt either the ILY^{ml}-like scenario or the PFO-like UDP conformation, including the arginine-to-L1 loop hydrogen bond.

DISCUSSION

Here we have presented the first crystal structure of VLY^{ml}, in complex with $CD59^{D22A}$ (Figure 1). We find that $CD59^{D22A}$ binds to one site in D4 of the toxin, reminiscent of the primary binding site observed in the published low-resolution (3.5 Å) structure of ILY^{ml}-CD59 (Johnson et al., 2013). To perform a detailed comparative study of the VLY^{ml} structure, we determined a higher-resolution structure of the ILY^{ml}-$CD59^{D22A}$ complex and a structure of uncomplexed ILY^{ml} (Figure 1). Extensive attempts to crystallize VLY^{ml} alone were unsuccessful. We saw no evidence of a second $CD59^{D22A}$ binding site in our VLY^{ml}-$CD59^{D22A}$ or ILY^{ml}-$CD59^{D22A}$ structures, which was supported by SAXS analysis of the ILY^{ml}-$CD59^{D22A}$ complex in solution (Figure 3). Although many of the interactions between toxin and $CD59^{D22A}$ are conserved between the VLY^{ml} and ILY^{ml} complexes there are some differences (Figure 2), which explains the variation in affinity for soluble $CD59^{D22A}$ between the two toxins reported herein (Figure S4).

Role of the UDP Loop in Initial Membrane Interactions

There are now a total of four available crystal structures, with seven independent views, of ILY alone or in complex with CD59 (Johnson et al., 2013; Polekhina et al., 2005). Remarkably, superimposition of D4 of all seven structures reveals that the UDP loop adopts a similar conformation, as does the L1 cholesterol-binding loop, in all of them, despite the different crystal packing (Figure 4A). Particularly notable is that the UDP loop side chain of R495 points out into solution and hydrogen bonds to E492, also from the UDP loop. In our previous work we showed that mutation of either residue to alanine has no effect on ILY membrane binding (Polekhina et al., 2005). In all the available structures of non-CD59-

dependent CDCs, of which PFO is the archetype, the equivalent arginine residue points toward the backbone of the L1 loop (and in many cases is within hydrogen-bonding distance). Mutation of the arginine to alanine in PFO results in a decrease in membrane binding, whereas mutation of the glutamic acid to alanine has no effect on binding. Most interestingly, in our two views of VLY^{ml} in the VLY^{ml}-$CD59^{D22A}$ complex presented here, the UDP loop of one monomer adopts a conformation similar to that seen in ILY^{ml} and the equivalent arginine interacts with the same glutamic acid (Figure 4C). However, in the other monomer the UDP loop adopts a conformation closer to that seen in PFO and the key arginine residue interacts with the L1 loop, as occurs in PFO (Figure 4B). Although a similar mutational study of VLY^{ml} has not been reported, it is known that VLY^{ml} can bind to cholesterol-rich membranes of non-human cells, resulting in the formation of oligomers and hemolysis (Zilnyte et al., 2015). Thus VLY^{ml} activity can bypass the need for human $CD59^{D22A}$ as a receptor but not cholesterol, consistent with our observation that VLY^{ml} can adopt UDP-loop interactions that are either ILY^{ml}-like or PFO-like, reflecting this Janus-like behavior. All these data are consistent with a model of membrane binding in which the arginine interaction with the L1 loop is a prerequisite for efficient L1 binding to membrane cholesterol. Indeed, mutation of the arginine to any other residue in PFO leads to a dramatic loss of activity with at least 50% decrease in binding (Dowd et al., 2012). Our modeling suggests that the conformation of the L1 loop is critical for cholesterol recognition and that the arginine interaction with the backbone ensures a correct conformation for initial binding of cholesterol. In the CD59-dependent CDCs, cholesterol binding is not essential in the first step as they can bind to membranes via their CD59 receptor. Thus there is no need for the arginine “trigger” residue to be locking the L1 loop in the proper conformation for cholesterol binding. But why do the CD59-dependent CDCs require a proline residue in the UDP loop, located between the arginine and glutamic residue? We believe that the proline residue increases the tendency for the side chains of these two charged residues to form a hydrogen bond and thus inhibit cholesterol binding in the absence of CD59 binding, as the L1 loop is not fixed in the correct conformation. A mutagenesis study showed that mutating the ILY UDP sequence to that of PFO (G485E, A486C, P493W, or just A486C and P493W) caused a loss of human-specific hemolytic activity and changed the mutant ILY sensitivity to cholesterol from none in ILY^{wt} to inhibition by low cholesterol concentrations in the mutants (Nagamune et al., 2004). Thus the proline residue in CD59-dependent CDCs appears to enhance CD59 binding at the expense of cholesterol binding.

Role of the UDP Loop in Early Oligomer Formation

ILY^{ml} (Johnson et al., 2013), listerolysin (LLO) (Koster et al., 2014), and PLY (Lawrence et al., 2015; Marshall et al., 2015) form linear oligomers in the crystal, and these oligomers likely represent a very early stage in formation of the CDC pore. The ILY^{ml} linear oligomer probably represents the earliest stage of monomer-monomer interactions. As there are very few contacts between ILY^{ml} molecules, the LLO oligomer seems to represent an intermediate state whereas the PLY linear oligomer has much more extensive interactions (Lawrence et al., 2015). Importantly, the progression from the “loose” oligomer seen in ILY^{ml} to the tight oligomer in PLY is accompanied by intermolecular interactions of the UDP loop between neighboring monomers, including a bifurcated hydrogen bond from the glutamic acid and arginine of the UDP loop in one protomer to an arginine residue at the top

the L3 loop in the adjacent monomer. This latter observation explains why the PFO R468A mutant cannot oligomerize (Dowd et al., 2012). A striking feature of the published ILY^{ml}-CD59 structure is that the intermolecular contacts include contributions from CD59: thus, a CD59 molecule from one complex interacts with D4 of the neighboring complex, suggesting that the receptor plays a role in the formation of the linear oligomer for CD59-dependent CDCs (Lawrence et al., 2015), but there are no intermolecular contacts between the UDP loops. Nor are there intermolecular UDP-loop contacts in linear and prepore oligomer models of VLY^{ml} (Figure 5). Thus it is possible that the UDP loop is not required for oligomerization contacts in these CDCs, as CD59 performs this role. We have found that knockouts of the cholesterol-binding motif in ILY did not block oligomerization but did block pore formation, so cholesterol binding was not required for prepore formation (Farrand et al., 2015; Giddings et al., 2004). Also, cholesterol binding by ILY cannot take place on natural membranes prior to its interaction with CD59 (Giddings et al., 2004). It appears that the UDP and L1 loops do not play any role in the initial stages of CD59-dependent CDC activity.

CD59 Detachment Mechanism

The rotation of D4 with respect to the main body of the protein seen in VLY^{ml} when compared with other CDCs is of particular interest. Assembly of our ILY^{ml}-CD59^{D22A} and VLY^{ml}-CD59^{D22A} complexes into linear oligomers based on the available linear oligomer crystal structures shows that in ILY^{ml}-CD59^{D22A} there are stabilizing interactions between the tip of the D4 β tongue and the adjacent CD59^{D22A} molecule (Figure 5A), as seen in the different crystal forms of the published structure (Johnson et al., 2013), which persist in the prepore model (Figure 5C). The VLY^{ml}-CD59^{D22A} complex, however, shows a loss of interaction between each VLY^{ml} monomer and the adjacent CD59^{D22A} when assembled into a linear oligomer (Figure 5B) and steric overlap between them in the prepore (Figure 5D). It is known that the assembly of ILY prepores retains CD59 as an anchor to the membrane (LaChapelle et al., 2009), but that on conversion to a pore the CD59 molecules are released. Our structures and MD simulations indicate that the conformation of VLY^{ml} in the VLY^{ml}-CD59^{D22A} complex may represent an intermediate orientation of the CDC as the switch occurs from the CD59-bound prepore toward the pore oligomeric structure. In representing an intermediate structure in this transition, there is what appears to be a domain swap occurring between adjacent VLY^{ml} monomers (Figure 5D). The twist of D4 with respect to the rest of the protein moves the D4 β tongue into interaction with the bottom of D2 of the adjacent monomer (Figure 5D). This observation from manual assembly of oligomers using the static crystal structure of the VLY^{ml}-CD59^{D22A} complex is supported by structural changes that occur in MD simulations of the CD59 complexes of both VLY and ILY. In particular, in ILY there is an electrostatic interaction between the β tongue of D4 and the base of D2 between residues R92 and E448 (Figure 5C). During MD simulations of the ILY-CD59 complex the interaction is broken, with E448 instead reorienting to interact with K65 from the bound CD59 molecule. Breaking the D4-D2 interaction within ILY and establishing an additional CD59-D4 interaction in its place frees domains 1–3 of the CDC to rotate with respect to D4. The formation of oligomeric complexes involving domain swapping is a well-established mechanism exploited by evolution to stabilize protein complexes (Liu and Eisenberg, 2002).

In summary, the functions of initial membrane attachment and formation of oligomers in the CD59-dependent CDCs are facilitated by the receptor at the expense of the UDP and L1 loops that are used for these functions in other CDCs. It appears that in the evolution of human CD59 specificity, replacement of a tryptophan residue by a proline in the UDP motif has promoted the breakage of the key interaction between the UDP and L1 cholesterol-sensing loops, possibly disfavoring cholesterol binding at the expense of CD59 binding. Interestingly, the VLY^{ml} structure revealed that it can adopt at least two UDP-loop conformations that either retain or disrupt the interaction between the two loops. This may explain why VLY can bind to either human CD59-bearing target cells or to cholesterol-rich non-human cells. The observation of a highly twisted VLY^{ml} monomer in the crystal structure, together with MD simulations, suggests a mechanism for how CD59 might become dislodged after prepore formation, and suggests that disruption of the D4-D2 interface might be a key event in transmitting the allosteric signal from D4 to unfurl the transmembrane regions in D3 for membrane insertion.

EXPERIMENTAL PROCEDURES

Cloning, Expression, and Purification

The *Escherichia coli* codon optimized VLY gene construct has been previously described (Gelber et al., 2008). VLY coding sequence A31–D516 was amplified by PCR and the monomer-locked form, containing mutations T333C and I348C, was made by mutagenesis. The monomer-locked mutant of ILY has been previously described (LaChapelle et al., 2009). CD59 was amplified from an IMAGE:4776621 cDNA clone. Point mutation D22A, known to enhance affinity for ILY (Wickham et al., 2011), was introduced by mutagenesis. All constructs were expressed in *E. coli*. $CD59^{D22A}$ complexes were made by mixing each CDC with $CD59^{D22A}$ in a 1:3 molar ratio followed by dialysis and SEC.

Crystallizations

Optimization of crystallization conditions was performed using the hanging-drop vapor diffusion method. For VLY^{ml}, drops of 1 μl of complex (2.65 mg/ml) mixed with an equal volume of precipitant were hung over 0.5 ml of well solution of 0.1 M ammonium acetate, 17% polyethylene glycol (PEG) 10,000, and 0.1 M Bis-Tris (pH 5.5). $MgCl_2$ (10 mM) was added to the drop only. For ILY^{ml}, 1 μl of complex was mixed with an equal volume of precipitant and hung over 0.5 ml of well solution of 10% (w/v) PEG 8000, 0.2 M zinc acetate, 100 mM 2-(N-morpholino)ethanesulfonic acid (pH 6.0), and 1 mM copper sulfate. Crystallization of free monomer-locked ILY^{ml} was performed using the same protocol as previously reported for wild-type ILY^{ml} (Polekhina et al., 2005).

Data Collection, Structure Determination, and Refinement

Data were collected at the Australian Synchrotron. Data and refinement statistics are listed in Table 1.

VLY^{ml}-$CD59^{D22A}$

The collected data were processed using XDS (Kabsch, 2010). Molecular replacement was performed using PHASER (McCoy et al., 2007). The search model was a low-resolution (~4

Å) unpublished structure of VLY^{ml}-$CD59^{D22A}$ determined from a different crystal form in-house.

Monomer-Locked ILY^{ml}

Data processing was performed using XDS (Kabsch, 2010). A molecular replacement solution was found with a monomer of wild-type ILY (Polekhina et al., 2005) as a search model and was built and refined as described above.

ILY^{ml}-$CD59^{D22A}$ Complex

The data were processed using the programs iMOSFLM and SCALA (Winn et al., 2011). A molecular replacement solution was obtained using a search model consisting of D1to D3 of ILY^{ml} (PDB: 1S3R). Subsequently D4 was found by fixing the solution obtained for D1 to D3. $CD59^{D22A}$ (based on PDB: 4BIK) was located during another round of molecular replacement.

Small-Angle X-Ray Scattering

SAXS data were collected on the SAXS/WAXS beamline at the Australian Synchrotron (Table S1), in static and SEC mode (Kirby et al., 2013). In SEC-SAXS mode, samples (48 µl at 6 mg/ml in 20 mM HEPES [pH 7.2] and 150 mM NaCl) were run with a Wyatt Technology WTC-050N5G SEC column equilibrated in the same buffer. Data acquisition and reduction analysis were carried out with Australian Synchrotron scatterBrain 9-1_0 software (Kirby et al., 2013). Statistical analysis of the goodness of fit of theoretical scattering profiles to experimental SAXS data and comparisons of the fits of SAXS data were performed as described in Mills et al. (2009).

Microscale Thermophoresis

Microscale thermophoresis solution binding studies between ILY^{wt} and $CD59^{D22A}$ and VLY^{wt} and $CD59^{D22A}$ were performed using standard protocols on a Monolith NT.115 (Nanotemper Technologies). $CD59^{D22A}$ was labeled with a Dylight 650 Antibody labeling kit (Thermo Scientific) according to the manufacturer's instructions. ILY^{wt} and VLY^{wt} were diluted in a 2-fold dilution series from 48 µM to 0.14 nM in 20 mM HEPES (pH 7.2), 150 mM NaCl, 0.05 mg/ml BSA, and 0.1% Tween 20. Each dilution was mixed 1:1 (v/v) with 10 ml of 40 nM Dylight 650-labeled $CD59^{D22A}$. Final reaction concentrations were 20 nM labeled $CD59^{D22A}$ with 0.07 nM to 6 µM for ILY^{wt} and 0.07 nM to 24 µM for VLY^{wt}. Assays were conducted in NanoTemper standard capillaries at 90% red LED power and 40% laser power, then heated for 30 s, followed by 5 s of cooling. All experiments were performed with a minimum of four independent replicates.

Affinity, K_D, was quantified by analyzing the change in normalized fluorescence (Fnorm = fluorescence after thermophoresis/initial fluorescence) as a function of the concentration of the titrated protein. The percentage of ILY^{wt} or VLY^{wt} bound (ΔFnorm/amplitude 3 100) was plotted against the concentration of protein and the experimental data points were fit with a sigmoidal function using GraphPad Prism (version 6), and the two curves were compared for statistical significance with the extra-sum-of-squares F test. Data are expressed as means and SEM.

Molecular Modeling

All simulations were conducted with NAMD 2.10 (Phillips et al., 2005). Five replicate production runs of each model were run for 100 ns. The ILY-CD59 model was based on the published structure (PDB: 4BIK) while the VLY structure was based on the one described here.

Supplementary Material

Refer to Web version on PubMed Central for supplementary material.

Acknowledgments

This research was partly undertaken on the MX2 and SAXS/WAXS beamlines at the Australian Synchrotron (Clayton, Victoria), and we thank the beamline staff for their assistance. This work was supported by an Australian Research Council Discovery Grant DP160101874 to M.W.P. MD simulations were supported by a grant from the Victorian Life Sciences Computation Initiative number VR0021 on its Peak Computing Facility (University of Melbourne), an initiative of the Victorian Government and by resources provided by the Pawsey Supercomputing Centre with funding from the Australian Government and the Government of Western Australia. This work was also supported by NIH grant AI037657 to R.K.T. Funding from the Victorian Government Operational Infrastructure Support Scheme to St Vincent's Institute is acknowledged. M.W.P. is a National Health and Medical Research Council of Australia Research Fellow.

REFERENCES

Dowd KJ, Farrand AJ, Tweten RK. The cholesterol-dependent cytolysin signature motif: a critical element in the allosteric pathway that couples membrane binding to pore assembly. PLoS Pathog. 2012; 8:e1002787. [PubMed: 22792065]

Farrand AJ, LaChapelle S, Hotze EM, Johnson AE, Tweten RK. Only two amino acids are essential for cytolytic toxin recognition of cholesterol at the membrane surface. Proc. Natl. Acad. Sci. USA. 2010; 107:4341–4346. [PubMed: 20145114]

Farrand AJ, Hotze EM, Sato TK, Wade KR, Wimley WC, Johnson AE, Tweten RK. The cholesterol-dependent cytolysin membrane-binding interface discriminates lipid environments of cholesterol to support beta-barrel pore insertion. J. Biol. Chem. 2015; 290:17733–17744. [PubMed: 26032415]

Gelber SE, Aguilar JL, Lewis KL, Ratner AJ. Functional and phylogenetic characterization of Vaginolysin, the human-specific cytolysin from Gardnerella vaginalis. J. Bacteriol. 2008; 190:3896–3903. [PubMed: 18390664]

Giddings KS, Johnson AE, Tweten RK. Redefining cholesterol's role in the mechanism of the cholesterol-dependent cytolysins. Proc. Natl. Acad. Sci. USA. 2003; 100:11315–11320. [PubMed: 14500900]

Giddings KS, Zhao J, Sims PJ, Tweten RK. Human CD59is a receptor for the cholesterol-dependent cytolysin intermedilysin. Nat. Struct. Mol. Biol. 2004; 11:1173–1178. [PubMed: 15543155]

Johnson S, Brooks NJ, Smith RA, Lea SM, Bubeck D. Structural basis for recognition of the pore-forming toxin intermedilysin by human complement receptor CD59. Cell Rep. 2013; 3:1369–1377. [PubMed: 23665225]

Kabsch W. XDS. Acta Crystallogr. D Biol. Crystallogr. 2010; 66:125–132.

Kirby NM, Mudie ST, Hawley AM, Cookson DJ, Mertens HDT, Cowieson N, Samardzic-Boban V. A low-background-intensity focusing small-angle X-ray scattering undulator beamline. J. Appl. Crystallogr. 2013; 46:1670–1680.

Koster S, van Pee K, Hudel M, Leustik M, Rhinow D, Kuhlbrandt W, Chakraborty T, Yildiz O. Crystal structure of listeriolysin O reveals molecular details of oligomerization and pore formation. Nat. Commun. 2014; 5:3690. [PubMed: 24751541]

LaChapelle S, Tweten RK, Hotze EM. Intermedilysin-receptor interactions during assembly of the pore complex: assembly intermediates increase host cell susceptibility to complement-mediated lysis. J. Biol. Chem. 2009; 284:12719–12726. [PubMed: 19293153]

Lawrence MC, Colman PM. Shape complementarity at protein/ protein interfaces. J. Mol. Biol. 1993; 234:946–950. [PubMed: 8263940]

Lawrence SL, Feil SC, Morton CJ, Farrand AJ, Mulhern TD, Gorman MA, Wade KR, Tweten RK, Parker MW. Crystal structure of Streptococcus pneumoniae pneumolysin provides key insights into early steps of pore formation. Sci. Rep. 2015; 5:14352. [PubMed: 26403197]

Liu Y, Eisenberg D. 3D domain swapping: as domains continue to swap. Protein Sci. 2002; 11:1285–1299. [PubMed: 12021428]

Marshall JE, Faraj BH, Gingras AR, Lonnen R, Sheikh MA, El-Mezgueldi M, Moody PC, Andrew PW, Wallis R. The crystal structure of pneumolysin at 2.0 Å resolution reveals the molecular packing of the pre-pore complex. Sci. Rep. 2015; 5:13293. [PubMed: 26333773]

McCoy AJ, Grosse-Kunstleve RW, Adams PD, Winn MD, Storoni LC, Read RJ. Phaser crystallographic software. J. Appl. Crystallogr. 2007; 40:658–674. [PubMed: 19461840]

Mills RD, Trewhella J, Qiu TW, Welte T, Ryan TM, Hanley T, Knott RB, Lithgow T, Mulhern TD. Domain organization of the monomeric form of the Tom70 mitochondrial import receptor. J. Mol. Biol. 2009; 388:1043–1058. [PubMed: 19358854]

Nagamune H, Ohnishi C, Katsuura A, Fushitani K, Whiley RA, Tsuji A, Matsuda Y. Intermedilysin, a novel cytotoxin specific for human cells secreted by *Streptococcus intermedius* UNS46 isolated from a human liver abscess. Infect Immun. 1996; 64:3093–3100. [PubMed: 8757839]

Nagamune H, Ohkura K, Sukeno A, Cowan G, Mitchell TJ, Ito W, Ohnishi O, Hattori K, Yamato M, Hirota K, et al. The human-specific action of intermedilysin, a homolog of streptolysin O, is dictated by domain 4 of the protein. Microbiol. Immunol. 2004; 48:677–692. [PubMed: 15383705]

Phillips JC, Braun R, Wang W, Gumbart J, Tajkhorshid E, Villa E, Chipot C, Skeel RD, Kale L, Schulten K. Scalable molecular dynamics with NAMD. J. Comput. Chem. 2005; 26:1781–1802. [PubMed: 16222654]

Polekhina G, Giddings KS, Tweten RK, Parker MW. Insights into the action of the superfamily of cholesterol-dependent cytolysins from studies of intermedilysin. Proc. Natl. Acad. Sci. USA. 2005; 102:600–605. [PubMed: 15637162]

Ramachandran R, Heuck AP, Tweten RK, Johnson AE. Structural insights into the membrane-anchoring mechanism of a cholesterol-dependent cytolysin. Nat. Struct. Biol. 2002; 9:823–827. [PubMed: 12368903]

Rossjohn J, Feil SC, McKinstry WJ, Tweten RK, Parker MW. Structure of a cholesterol-binding, thiol-activated cytolysin and a model of its membrane form. Cell. 1997; 89:685–692. [PubMed: 9182756]

Shatursky O, Heuck AP, Shepard LA, Rossjohn J, Parker MW, Johnson AE, Tweten RK. The mechanism of membrane insertion for a cholesterol-dependent cytolysin: a novel paradigm for pore-forming toxins. Cell. 1999; 99:293–299. [PubMed: 10555145]

Shepard LA, Heuck AP, Hamman BD, Rossjohn J, Parker MW, Ryan KR, Johnson AE, Tweten RK. Identification of a membrane-spanning domain of the thiol-activated pore-forming toxin *Clostridium perfringens* perfringolysin O: an alpha-helical to beta-sheet transition identified by fluorescence spectroscopy. Biochemistry. 1998; 37:14563–14574. [PubMed: 9772185]

Shewell LK, Harvey RM, Higgins MA, Day CJ, Hartley-Tassell LE, Chen AY, Gillen CM, James DB, Alonzo F 3rd, Torres VJ, et al. The cholesterol-dependent cytolysins pneumolysin and streptolysin O require binding to red blood cell glycans for hemolytic activity. Proc. Natl. Acad. Sci. USA. 2014; 111:E5312–E5320. [PubMed: 25422425]

Soltani CE, Hotze EM, Johnson AE, Tweten RK. Specific protein-membrane contacts are required for prepore and pore assembly by a cholesterol-dependent cytolysin. J. Biol. Chem. 2007; 282:15709–15716. [PubMed: 17412689]

Tabata A, Ohkura K, Ohkubo Y, Tomoyasu T, Ohkuni H, Whiley RA, Nagamune H. The diversity of receptor recognition in cholesterol-dependent cytolysins. Microbiol. Immunol. 2014; 58:155–171. [PubMed: 24401114]

Tilley SJ, Orlova EV, Gilbert RJ, Andrew PW, Saibil HR. Structural basis of pore formation by the bacterial toxin pneumolysin. Cell. 2005; 121:247–256. [PubMed: 15851031]

Tweten RK. Cholesterol-dependent cytolysins, a family of versatile pore-forming toxins. Infect Immun. 2005; 73:6199–6209. [PubMed: 16177291]

Volkov VV, Svergun DI. Uniqueness of ab initio shape determination in small-angle scattering. J. Appl. Crystallogr. 2003; 36:860–864.

Wade KR, Hotze EM, Kuiper MJ, Morton CJ, Parker MW, Tweten RK. An intermolecular electrostatic interaction controls the prepore-to-pore transition in a cholesterol-dependent cytolysin. Proc. Natl. Acad. Sci. USA. 2015; 112:2204–2209. [PubMed: 25646411]

Wickham SE, Hotze EM, Farrand AJ, Polekhina G, Nero TL, Tomlinson S, Parker MW, Tweten RK. Mapping the intermedilysin-human CD59 receptor interface reveals a deep correspondence with the binding site onCD59 for complement binding proteins C8alpha and C9. J. Biol. Chem. 2011; 286:20952–20962. [PubMed: 21507937]

Winn MD, Ballard CC, Cowtan KD, Dodson EJ, Emsley P, Evans PR, Keegan RM, Krissinel EB, Leslie AG, McCoy A, et al. Overview of the CCP4 suite and current developments. Acta Crystallogr. D Biol. Crystallogr. 2011; 67:235–242.

Zilnyte M, Venclovas C, Zvirbliene A, Pleckaityte M. The cytolytic activity of vaginolysin strictly depends on cholesterol and is potentiated by human CD59. Toxins (Basel). 2015; 7:110–128. [PubMed: 25590277]

Zvirbliene A, Pleckaityte M, Lasickiene R, Kucinskaite-Kodze I, Zvirblis G. Production and characterization of monoclonal antibodies against vaginolysin: mapping of a region critical for its cytolytic activity. Toxicon. 2010; 56:19–28. [PubMed: 20298711]

Highlights

- VLY and ILY recognize their receptor in related but not identical ways
- A key proline residue may promote CD59 binding indirectly
- A domain-swapping model could explain CD59 detachment

In Brief

Lawrence et al. present crystal structures of the cholesterol-dependent cytolysins vaginolysin and intermedilysin bound to their receptor, human CD59. The structures provide new insights into how this family of toxins pierces eukaryotic cell membranes to form gigantic pores.

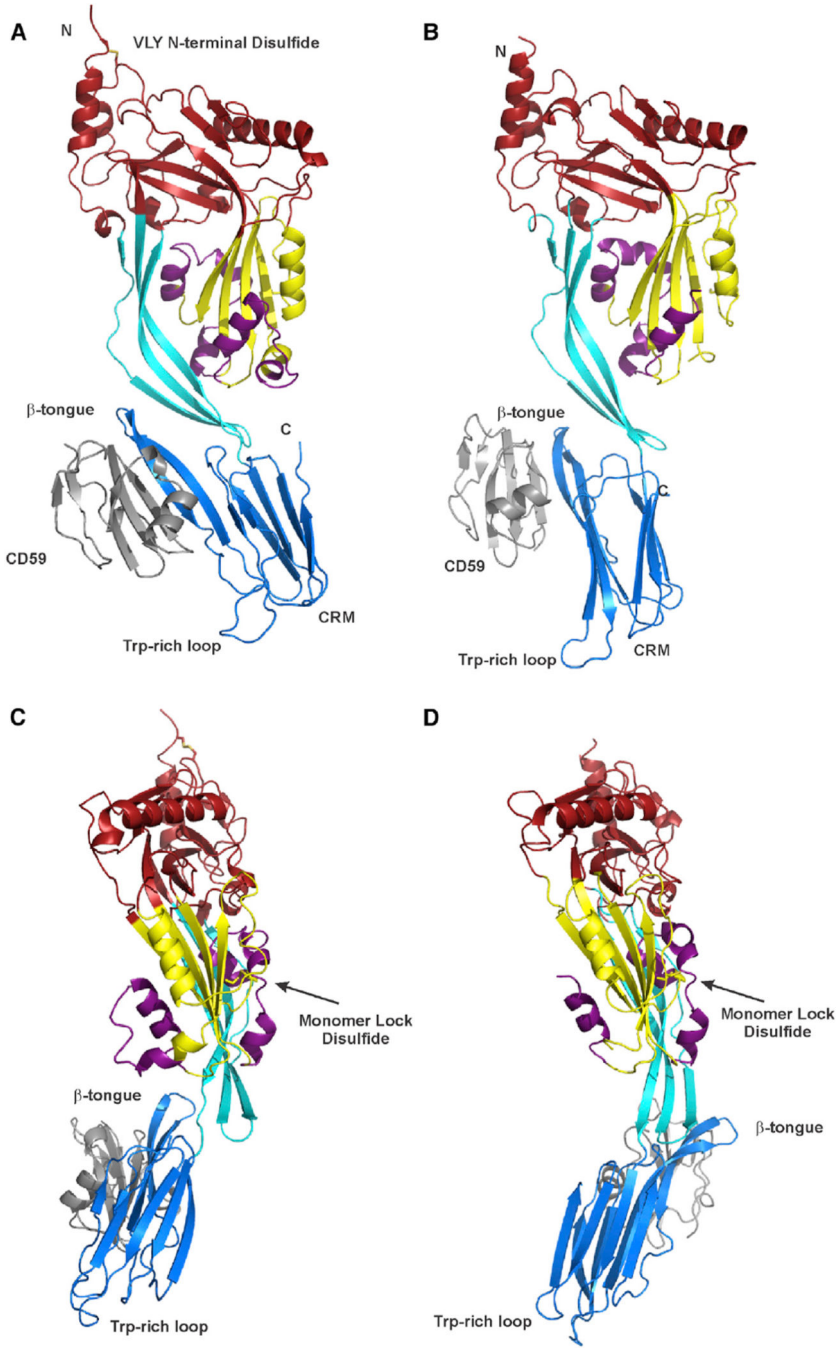

Figure 1. Crystal Structures of the CDC-CD59 Complexes

The structures are shown in ribbon representation. D1 is colored red, D2 cyan, D3 yellow, and D4 dark blue. The TMH1 and TMH2 regions are colored mauve. Two of the membrane-sensing loops of D4 (Trp-rich UDP loop and L1 loop housing the cholesterol-recognition motif) and the D4 β tongue are indicated. $CD59^{D22A}$ is gray.

(A) VLY^{ml}-$CD59^{D22A}$.

(B) ILY^{ml}-$CD59^{D22A}$.

(C) VLY^{ml}-$CD59^{D22A}$.

(D) ILY^{ml}-$CD59^{D22A}$.

See also Figures S1 and S3.

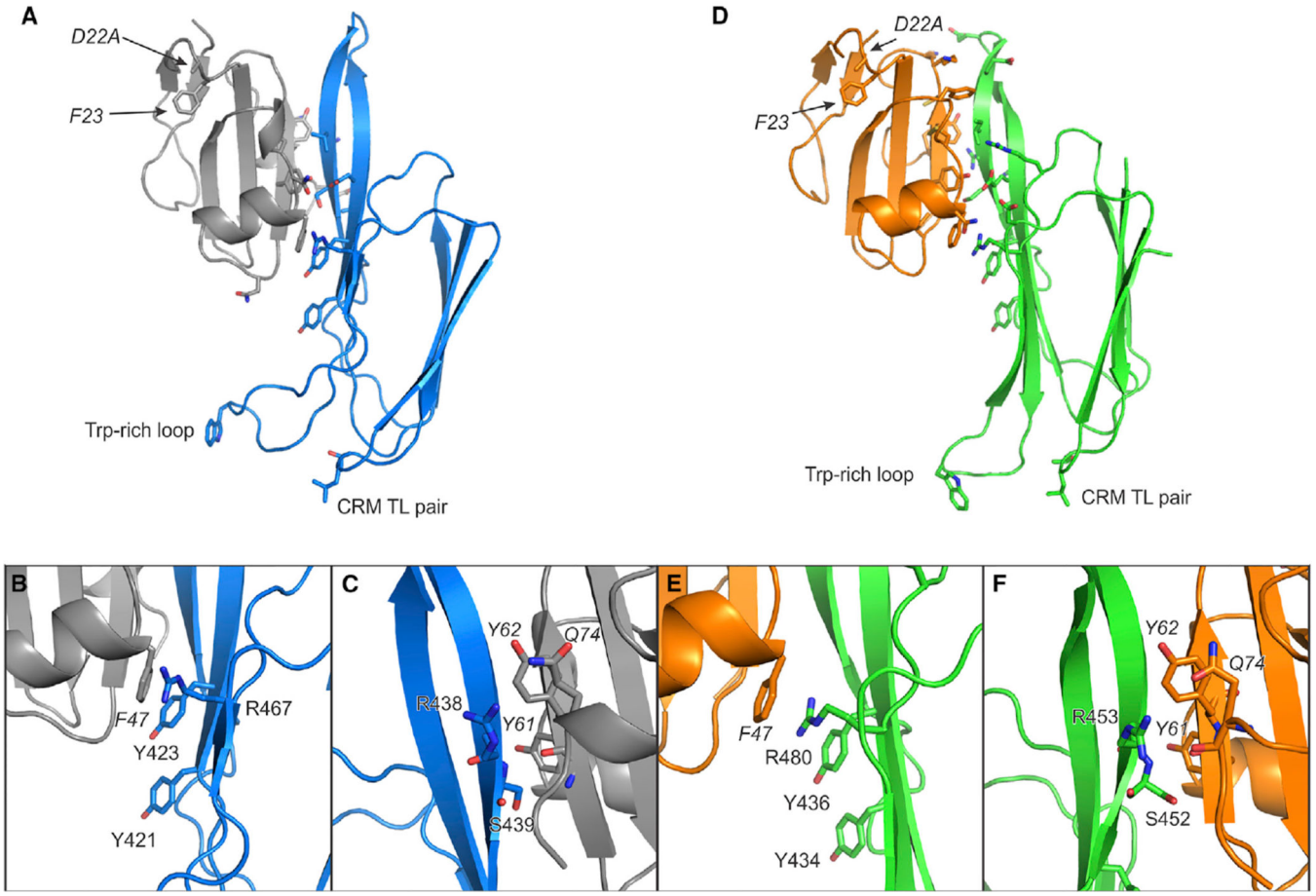

Figure 2. Detailed Views of the Interactions between CD59 and the CDCs

The proteins were oriented by superimposing the $CD59^{D22A}$ molecule of the VLY^{ml}-$CD59^{D22A}$ complex onto the $CD59^{D22A}$ of the ILY^{ml}-$CD59^{D22A}$ complex. Interfacial residues mentioned in the text are shown with key residues labeled, with those from $CD59^{D22A}$ in italics. The UDP loop is labeled with the Thr-Leu cholesterol-recognition motif (CRM) residues on L1 indicated.

(A–C) VLY^{ml} (blue) and $CD59^{D22A}$ (gray).

(D–F) ILY^{ml} (green) and $CD59^{D22A}$ (orange).

Close-up views are shown of the $CD59^{D22A}$-CDC interfaces for VLY^{ml} (B and C) and ILY^{ml} (E and F) with the Y-X-Y-X_{14}-R-S CD59-motif residues and their contact residues in $CD59^{D22A}$ labeled.

See also Figures S2, S5, and S6.

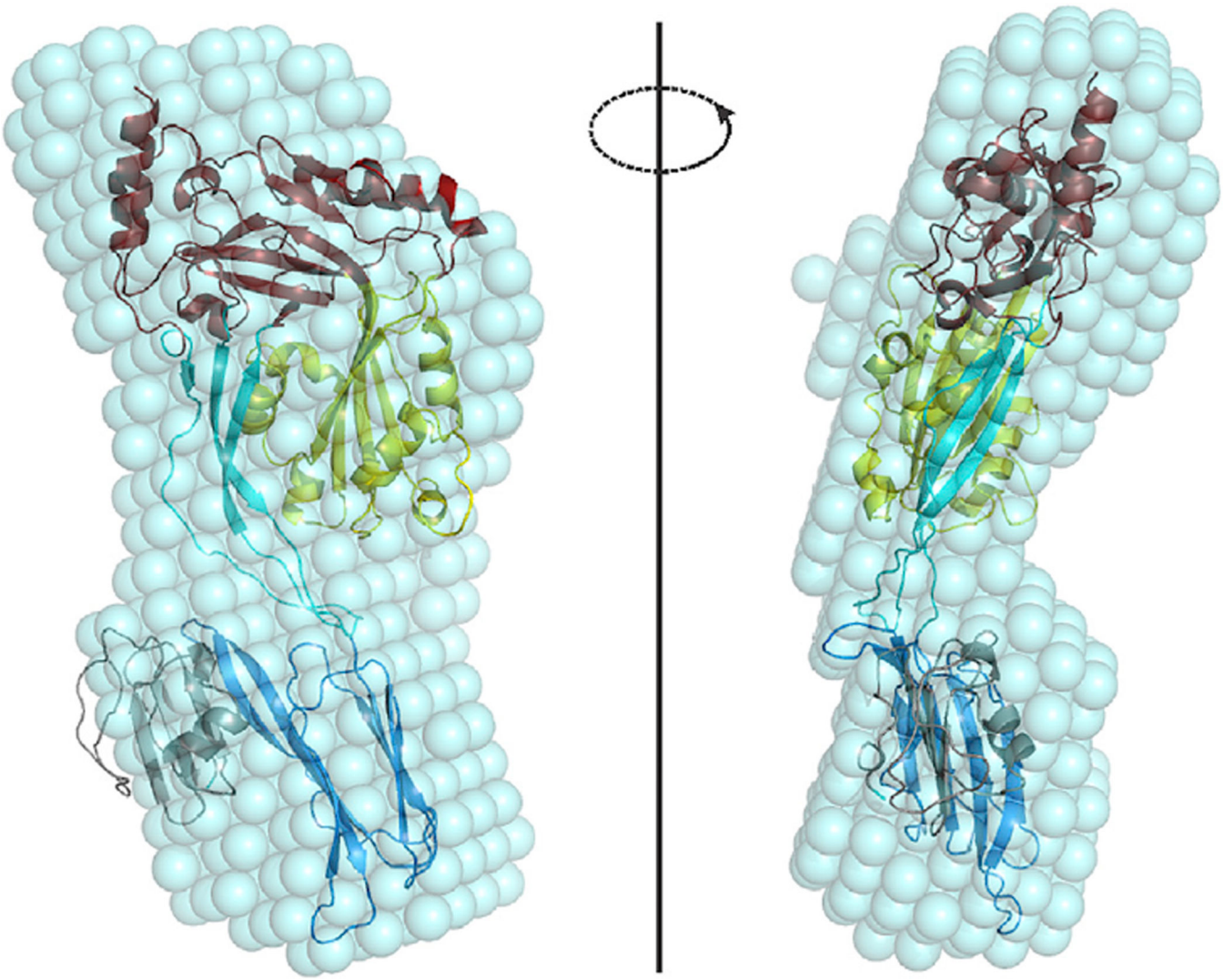

Figure 3. SAXS Analysis of the ILY^{ml}-CD59^{D22A} Complex

Orthogonal views of the optimal superposition of the best fitting SAXS-derived ab initio shape envelope with the ILY^{ml}-CD59^{D22A} crystal structure. The averaged filtered shape envelope from DAMAVER (Volkov and Svergun, 2003), derived from the best matching cluster of 8 DAMMIF models from a total of 30, is shown in cyan spheres and has been optimally superimposed on the ILY^{ml}-CD59^{D22A} structure. ILY^{ml} is colored as in Figure 1 (domains colors of red, yellow, cyan, and dark blue) and CD59^{D22A} in gray.

See also Figure S4.

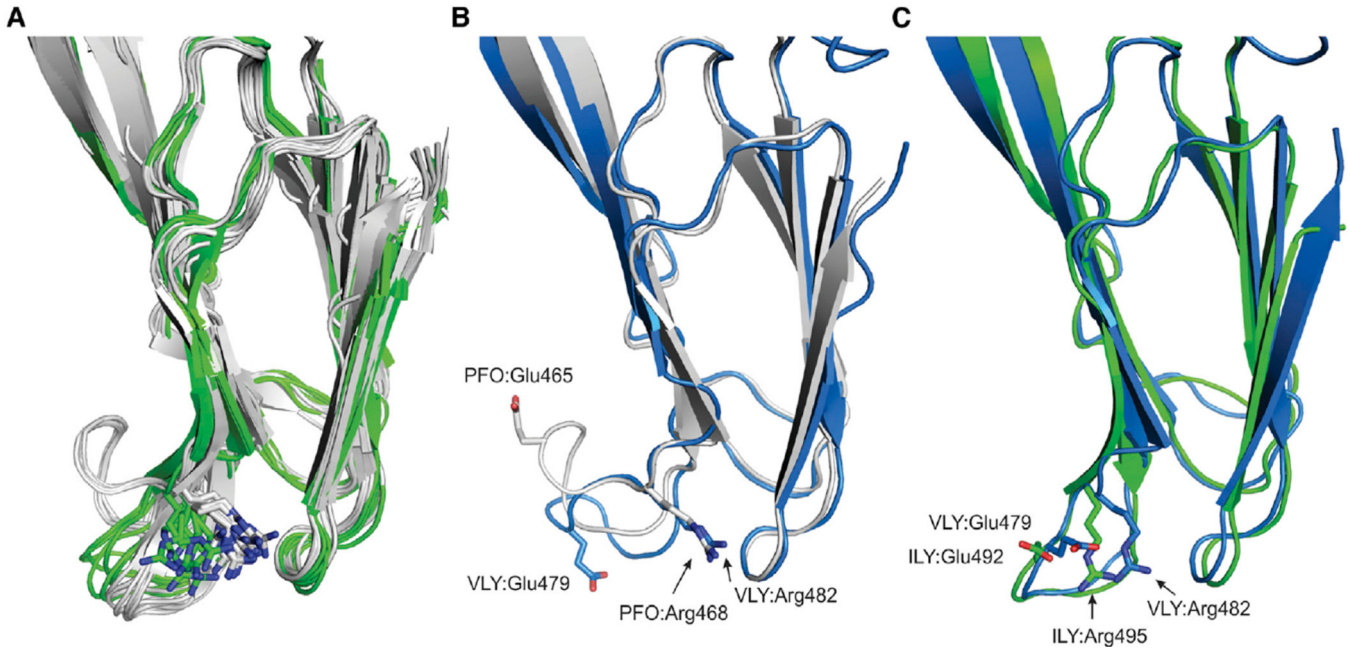

Figure 4. Superimposition of D4 of Available CDC Structures Showing the UDP and L1 Loops with Key Residues, Arginine and Glutamic Acid, from the UDP Loop

(A) Superimposition of all available CDC structures. Non-CD59 dependent CDCs are shown in gray and ILY structures in green.

(B) Superposition of VLY^{ml} chain A (blue) with PFO.

(C) Superposition of VLY^{ml} chain B with ILY.

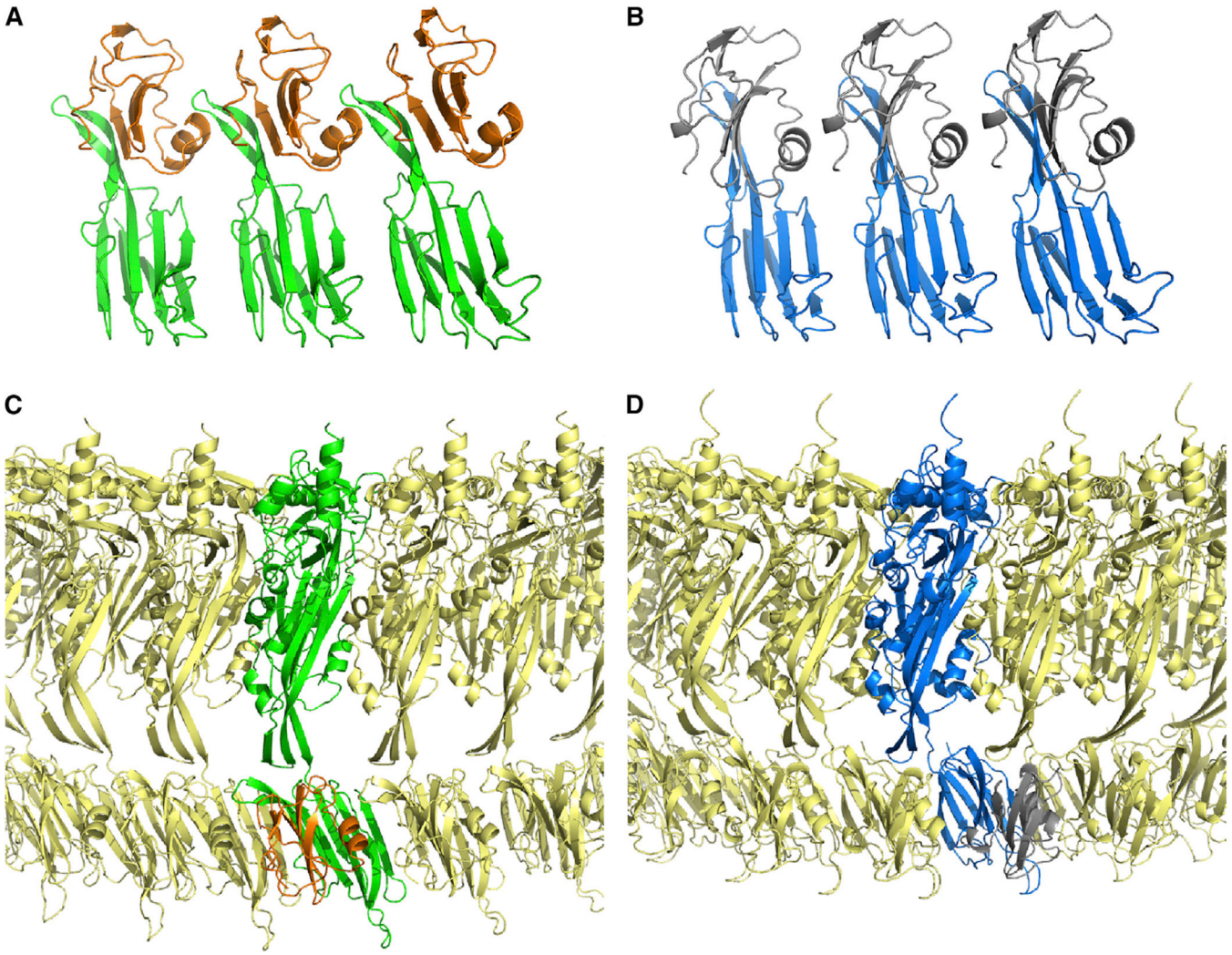

Figure 5. Models of ILY^{ml} and VLY^{ml} Linear Oligomers and Prepores

(A) ILY^{ml}-CD59^{D22A} linear oligomer modeled on the PLY oligomer (Lawrence et al., 2015; Marshall et al., 2015). ILY is shown in green and CD59 in orange.

(B) VLY^{ml} (Chain B)-CD59^{D22A} linear oligomer modeled on the PLY oligomer (Lawrence et al., 2015; Marshall et al., 2015). VLY is shown in blue and CD59 in gray.

(C) ILY^{ml}-CD59^{D22A} prepore modeled on the published PLY prepore (Tilley et al., 2005). One protomer of the complex is highlighted with ILY is shown in green and CD59 in orange.

(D) VLY^{ml}-CD59^{D22A} prepore modeled on the published PLY prepore (Tilley et al., 2005). One protomer of the complex is highlighted with VLY is shown in blue and CD59 in gray.

Table 1

Crystallographic Data and Refinement Statistics

	ILY^{ml}	**ILY^{ml}-CD59^{D22A}**	**ILY^{ml}-CD59^{D22A}**
Data Collection			
Temperature (K)	100	100	100
Space group	$P2_12_12$	$C222_1$	$P2_12_12$
Cell dimensions			
a (Å)	84.5	93.7	81.9
b (Å)	101.6	66.6	141.7
c (Å)	175.7	118.3	106.7
Resolution (Å)	2.9	2.7	2.4
No. of observations	502,239	102,547	219,340
No. of unique reflections	34,453	25,634	49,244
Redundancy	14.6 (13.4)	4.0 (4.1)	4.5 (4.5)
Data completeness (%)	98.8 (92.1)	99.6 (100)	99.9 (100)
I/σ_I	10.9 (2.7)	8.5 (2.6)	13.1 (1.5)
R_{pim} (%)	0.042 (0.34)	0.09 (0.35)	0.051 (0.54)
Refinement			
Non-hydrogen atoms			
Protein	7,914	4,205	8,665
Water	0	127	137
Ligands			
Metal ions	0	7	0
SO_4^{2-} ions	0	2	0
Resolution (Å)	2.9	2.7	2.4
R_{cryst} (%)	21.6	18.1	23.4
R_{free} (%)	27.8	25.0	27.3
Rmsd from ideality			
Bond lengths (Å)	0.017	0.016	0.003
Bond angles (Å)	1.9	1.6	0.7
Dihedrals (°)	19.0	17.3	13.3
Average *B* factor (Å^2)			
Main chain	59.5	36.5	55.8
Side chain	67.2	39.7	61.9
Water	–	29.1	50.6
Residues in allowed regions of the Ramachandran plot (%)	99.2	100	97.4

Values in parentheses are for the highest-resolution bin (approximately 0.1 Å width).